Synthesis and Characterization of MoS 2 Nanoflowers Decorated Amino Cellulose Derivatives: An Innovative Approach for Anticancer Therapeutics

Farzana Nazir
 National University of Science and Technology (NUST)

Areesha Khan
 National University of Science and Technology (NUST)

Iffat Ashraf
 National University of Science and Technology (NUST)

Faiza Lughmani
 National University of Science and Technology (NUST)

Bushra Rafiq
 National University of Science and Technology (NUST)

Mudassir Iqbal (✉ mudassir.iqbal@sns.nust.edu.pk)
 National University of Science and Technology (NUST)

Research Article

Abstract

Microcrystalline cellulose (MCC) was modified to amino cellulose (AC) derivatives, 6-deoxy-6-hydrazide cellulose, 6-deoxy-6-(N, N-diethyl) amine cellulose, and 6-deoxy-6-diethyltriamine cellulose (C-Hyd, C-DEA, and C-DETA). AC's were used as supporting material for the MoS_2 Nanoflowers (NFs) for the development of nanocomposites as cancer therapeutics. ACs-MoS_2 nanocomposites were analyzed by using spectroscopy, X-ray diffraction (XRD), Scanning Electron Microscopy (SEM)-EXS, and Zeta potential. MoS_2 NF loading, swelling, and degradation rate of ACs-MoS_2 nanocomposites have been investigated. ACs-MoS_2 nanocomposites were analyzed against four cancer cell lines NIH3T3, B16F10, MDA-MB-231, and MCF-7 cell lines by using presto blue and LIVE/DEAD staining. Cell viability assay and fluorescence microscopy against four cell lines revealed that all AC's-MoS_2 nanocomposites with 5wt% MoS_2 showed selective cytotoxicity for cancer cell lines as compared to normal fibroblast cell lines. Our findings revealed that amino cellulose derivatives loaded with MoS_2 could be efficient candidates for skin and breast cancer therapy.

1. Introduction

Cancer is one of the leading causes of death in the world. The presently available methods for cancer treatment are surgical removal of the tumor, chemical therapy, and radiotherapy. These treatments are partially effective because of side effects [1]. Nanomaterials have sizes in between the size of cells and molecules. Theoretically, precisely constructed nanomaterials, can realize the regulation of cell state and function just like organelles in cells. Nanomaterials have attracted much attention over the past two decades as cancer therapeutics. Currently, nanomedicine has shown promising potential as a cancer therapeutic. Nanomedicine involves the development of nanomaterials with unique surface chemistry and physical properties [2, 3].

Among nanomaterials, nanoflowers are characterized by distinct topographic features of layers, high surface-to-volume ratio as compared to spherical nanomaterials, and significant efficiency of surface reactions as compared to other nanomaterials [4]. Nanoflowers are used in biosensors, catalysis, and capsules but their main purpose is in biomedicine enzyme stabilizers. Metal-organic hybrid nanoflowers are widely used as enzymes and in cancer therapy [5, 6]. Molybdenum disulphide MoS_2 is a 2D semiconductor material that emerged as an attractive candidate for cancer treatment for instance, as a drug delivery agent, detection marker, biosensor, and imaging [7–9]. Unique features of MoS_2 such as controllable size, precise synthesis, easy integration, and functionalization with nanomaterials and biomolecules help in the development of cancer nanomedicine. Unlike other nanomaterials, such as gold and silver, which require upconversion, MoS_2 consists of the trace elements found in the human body. Molybdenum MoS_2 is found in enzymes such as xanthine oxidase, aldehyde oxidase, and sulfite oxidase. Moreover, Mo deficiency may lead to esophageal cancer and is effective in diabetes treatment [10]. In order to fully exploit the potential of MoS_2, MoS_2 is functionalized with soluble, biocompatible, biodegradebale, and functional polymers to obtain MoS_2 nanocomposites. MoS_2-nanocomposites are greener and a new class in cancer chemodynamic therapy [11, 12].

Cellulose is nature's most abundant, low-cost, hydrophilic, renewable, mechanically strong, biopolymer. [13]. Cellulose, its derivatives, and nanocomposites are usually biocompatible therefore, these are used in biomedical applications such as tissue engineering [13, 14], wound healing [15], cancer therapy [16], and drug delivery [17]. Hydroxyl groups in cellulose can be easily functionalized to obtain cellulose derivatives having modified surface chemistry for the adsorption of nanomaterials [18]. In recent years, amino functionalized cellulose derivatives (ACs)

have piqued the interest of researchers in biomedicine. ACs have higher stability, lower toxicity, and a positively charged surface which augments negatively charged nanoparticles to adsorb on its surface. AC's nanocomposites result in increased cell wall degradation and bactericidal activity [19]. AC's were used to prepare highly stable silver nanoparticles, deposited on the surfaces for antibacterial action [20]. In another case, the continuous release of silver ions from Ag nanoparticle-impregnated bacterial cellulose hybrid composites showed improved antibacterial activity with a quicker Ag^+ release profile [21]. Zhou. C have reported cellulose fibre based sensors with CeO_2 and Bi_2S_3@MoS_2 nanoflowers microfluidic paper for MiRNA [22]. Cellulose as a delivery system such as ethyl cellulose/chitosan/g-C3N4/MoS_2 core-shell nanofibers, successfully carries medications folic acid and doxorubicin into MCF-7 and HeLa cells [23].

In this study, we present synthesis of the novel AC's adsorbed with MoS_2 Nanoflowers (NF's). In first step, 6-Deoxy-6 AC's were prepared by tosylated intermediate of MCC. Then hydrazine, diethylamine, and diethyl tetraamine were substituted on cellulose backbone. In second step, the MoS_2 was adsorbed on the surface of these AC's to obtain a powdered nanocomposite. OH, and NH_2 groups served as a binding site for the MoS_2 by electrostatic attraction. Finally, the cytotoxicity of these nanocomposites was evaluated against the NIH3T3, B16F10, MDA-MB-231, and MCF-7 by using Presto blue and LIVE/DEAD staining.

2. Materials And Methods

2.1. Materials

Sodium molybdate dihydrate $Na_2MoO_4.2H_2O$, methylmercaptan sodium CH_4NaS, Microcrystalline (MCC), p-Toluenesulfonyl chloride, diethylamine (DEA), lithium Chloride Anhydrous (LiCl), were obtained from DAEJUNG, Korea. N,N-dimethyl acetamide (DMAc), triethylamine (TEA), hydrazinium hydroxide, diethylenetriamine (DETA), ethanol, hydrochloric Acid (HCl), nitric acid (HNO_3), dimethylsulfoxide (DMSO), and deionized water were procured from Sigma Aldrich. All reagents were of synthetic grade and were used without further purification. 1-butyl-3-methylimidazolium chloride (BMIM [Cl]), was prepared in laboratory. For cell culture all reagents DMEM, FBS, Penstrep, PBS, were obtained from Gibco, Thermo Fisher Scientific Inc, Waltham, MA, USA. NIH3T3, B16F10, MDA-MB-231 and MCF-7 cell lines were obtained from American Type Culture Collection (ATCC), (Manassas, VA, USA).

2.2. Method

2.2.1 MoS$_2$ nanoflower (NFs) synthesis

Single and few layer MoS_2 nanoflower (NFs) were prepared by an already reported hydrothermal process, as shown in Scheme 1b) [24]. Briefly, $Na_2MoO_4.2H_2O$ (1.44 g), and CH_4NaS (1.38g) powder were added in 2 mL (BMIM [Cl]). Next, above solution was titrated against dilute HCl. Resulting solution was agitated for 12 hours until a clear solution was formed. Then, clear solution was autoclaved at 220°C for 24 hours. After that, MoS_2 NFs with a black hue was filtered and washed in distilled water. The final product was stored in a capped glass bottle for further analysis. Synthesis of MoS2 NF's has been shown in Scheme 1b).

2.2.2. Preparation of Tosylated Cellulose (C$_{TOS}$)

Tosylated Cellulose(C_{TOS}) was prepared by a previously reported method [25]. Briefly, 5g dried MCC was dissolved in DMAc in the presence of LiCl, followed by p-Toluene sulfonyl chloride with TEA. C_{TOS} was obtained as a white

powder with 77% yield after precipitation and purification as shown in Scheme 1a).

2.2.3. Preparation of 6-Deoxy-Amine Functionalized Cellulose (AC's) by C$_{TOS}$

AC's synthesis was started by mechanically stirring previously prepared C$_{TOS}$ (2 g) in DMF (2mL) until dissolved. Next, 25 equivalents of the desired amines i.e., Hydrazinium hydroxide, Diethylamine, or Diethylenetriamine in DMF (10mL) were added separately to replace tosylate groups with amines. Different amines along with TEA (1mL) were added dropwise to viscous solution of C$_{TOS}$ at constant stirring at 90°C. Reaction was continued to progress for 24 hours under reflux. To obtain the product, the reaction mixture was dialyzed in deionized water and ethanol. The obtained polymeric product was collected by filtration and vacuum-dried at 50°C. Products obtained were 6-deoxy-6-hydrazide Cellulose, 6-deoxy-6-diethylamide Cellulose, and 6-deoxy-6-diethyltriamide named C-HYD, C-DEA, and C-DETA, respectively. The synthesis scheme of AC's synthesis from MCC is shown in Scheme 1a).

2.2.4 Fabrication of AC-MoS$_2$ NF's nanocomposites

For fabrication of the MoS$_2$ and AC nanocomposites as shown in Scheme 1c), MoS$_2$ NF's was added in 1, 3 and 5% in three different AC's separately. First, MoS$_2$ NF's were ultrasonicated in water for half an hour. Then, AC's were ultrasonicated in DMSO for half an hour. Dispersed MoS$_2$ NFs were added in the AC's in 1, 3 and 5 weight percentages. Resulting mixtures were agitated for 12 hours at 40°C before freeze drying to obtain the powdered nanocomposites.

2.3. Characterization

MoS$_2$ nanoflowers and AC-MoS$_2$ nanocomposites were characterized morphologically by SEM (JSM-64900) and an EDX spectrometer (JEOL USA, INC, MA, USA). The FTIR spectra were collected using a Bruker attenuated total reflectance Fourier transform infrared (ATR FT-IR) spectrophotometer (Bruker platinum ATR model Alpha spectrophotometer, Germany). 20mg samples were scanned to check the functionality at wave numbers ranging from 4000 to 400 cm^{-1}. All samples had their ^{1}HNMR spectra recorded at room temperature using Bruker AV400 spectrometer (Bruker corporation MA, USA). The ζ- potential plot was analyzed using the Zetasizer software PCS V.1.4 (Malvern Instruments, Malvern, UK). Utilizing the CKIC 5E-CHNS-2200 and CKIC 5E-IRS II elemental studies were carried out (CHANGSHA KAIYUAN INSTRUMENTS CO LTD, Changsha, China). X-ray Diffraction patterns of cellulose and its derivatives were recorded (D8 advance BRUKER, USA) over 2θ = 5−80° with Cu Kα radiation. For swelling analysis, 10mg sample in 1 mL of Dulbecco's phosphate-buffered saline (DPBS) was placed in Eppendorf tubes. After 24 hours in a shaker at 37°C, the samples were dried and weighed to calculate swelling ratios by following formula

$$SwellingRatio = \frac{Weight of the swollen sample - Weight of the dried sample}{Weight of the dried sample} \times 100$$

Degradation studies of samples were carried out by 20mg of sample with 1mL of the collagenase Type II enzyme. Samples were removed at specific time intervals and freeze dried at before weight measurements. Triplicate samples were used for each trial.

Cell culture: *In vitro* cytotoxicity of the synthesized cellulose derivatives was evaluated against four different cell lines according to a previous method. These cell lines were fibroblast cell line NIH3T3 (mouse embryo fibroblasts),

one cancer cell line B16F10 (mouse skin melanoma), and two breast cancer cell lines MDA-MB-231(human epithelial adenocarcinoma), and MCF-7 (human breast adenocarcinoma). Frozen Cell lines were passaged in DMEM supplemented with 10% FBS and 1% Penstrep five times at 37°C and humidified air with 5% CO_2. Cell viability and cytotoxicity index was evaluated by adding 30,000 cells/mL or 10,000 cells/cm^2 on a 96 well plate for each cell line maintained at standard conditions for a period of 24 h. Next day media was removed, and cells were washed with PBS to get rid of the debris or any dead cells. Then, cellulose its amine derivatives composites with MoS_2 NF's were added in DMEM. In first step the MoS_2 adsorption concenteration on AC's was varied to check the IC_{50} value based on MoS_2. For this MoS_2 concenteration was taken as 10, 20, 30, 40, 50, 60, 80, and 100 µg/mL. 100 µL of each nanocomposite was added in a 96 well plate and incubated in the same condition for the next 24 h (1 Day) to check the IC_{50}.

In another strategy anticancer activity of AC-MoS_2 (1, 3, and 5 wt% of MoS_2) against four cell lines was evaluated by using prestoblue assay for day 1 and day 3. Only an equivalent volume of fresh media was given to control cells. Cell viability and cytotoxicity index was evaluated by adding 30,000 cells/mL or 10,000 cells/cm^2 on a 96 well plate for each cell line for a period of 24 h. Next day media was removed, and 100 µL of each AC-MoS_2 (1, 3, and 5 wt% of MoS_2) in DMEM were added in 96well plate. PrestoBlue (10% PrestoBlue in DMEM). in DMEM was added in 96 well plate and incubated in the same condition for the next 24 h (1 Day) and 72 h (3 Days). Only an equivalent volume of fresh media was given to control cells. PrestoBlue (10% PrestoBlue in DMEM). cell viability Reagent was added on cells on day 1 and day 3 for 2 h. After 2 hrs media was added to 96 well plate to observe at fluorescence intensity excitation/emission 535−560/590−615 using a plate reader. analysis. All cell experiments were carried out in three independent experiments with triplicate samples. All data were presented here as an average ± standard deviation (S.D.), and p < 0.05 considered as significant difference. LIVE/DEAD Assay kit (mammalian cells). was used at day1 for visualizing live and dead cells. Cells were seeded on 24 well plate using same protocol as mentioned above. For control cells were added with complete media. After 24 hours contact with AC-MoS_2 nanocomposites cells were washed with PBS to remove any dead cells. Calcein AM and Ethidium homodimer-1 50 µL was added to each well. After 30−40 min in contact with LIVE/DEAD cells were observed using inverted fluorescence microscope (Zeiss Axio Observer Z1, Zeiss, Germany) at 494/517 nm for Calcein-AM and at 528/617 nm ethidium homodimer. Number of live cells were counted by Image J (US National Institutes of Health, USA) software and from four random fields of 3 replicates of samples. Live cell percentage was counted by dividing number of live cells by total number of cells. Four random field images were taken at 10 ×.

3. Results And Discussion

In the beginning MCC was coverted to C_{TOS} by an already reported method. Next, Amino cellulose derivatives (AC's) were prepared by a simple nucleophilic substitution reaction where C_{Tos} was replaced by three different amines to obtain C-Hyd, C-DEA, and C-DETA [25], as presented in scheme 1a). In next step, MoS2 NF's were synthesized as hsown in scheme 1b)

Finally, to obtain the AC-MoS_2 nanocomposites as shown in scheme 1c), AC's were decorated with MoS_2 on their surface by mixing the AC's solution with MoS_2 solution and subsequent freeze-drying to remove the solvent. Due to the presence of nitrogen as a donor atom, amino-functionalized cellulose now coordinated with MoS_2 NF's and improved their dispersal and stability on polymer surfaces.

Synthesized MoS$_2$ NF's nanoflowres, AC's and AC-MoS$_2$ were charav = chterized as follows to elucidate their potential as cancer therapeutics.

3.1 Structural Charachterization of MoS$_2$ NF's

MoS$_2$ NF's were prepared by the cost effective, high yield hydrothhermal method and charachterized by XRD, and Raman spectra as shown in Fig. 1a) and b). XRD pattern as shown in Fig. 1a) matches with the JCPDS card no. 37-1492 indicating single phase MoS$_2$ NFs. The characteristic XRD pattern was observed at 14.1°, 33.4°, 40.8°, and 57.8° corresponding to (002), (100), (103), and (110), respectively [26]. First peak belonging to (002) plane is broad, and is of low intensity which implicit that the synthesized MoS$_2$ NFs have an astounding fraction of single and few layer MoS$_2$ NF's [24]. The 002 peak showed a slight shifting of 0.45° which confers a little higher lattice spacing ~ 0.64 nm as compared to reported literature of 0.62 nm [27]. Increase in lattice spacing indicates uniaxial strain along (001) plane of MoS$_2$ NF's. MoS$_2$ NF's were further elucidated by raman spectroscopy as shown in of Fig. 1b). MoS$_2$ NF's clearly exhibit a shorter distance, uniform, and broad Raman band related to E^1_{2g} and A^1_{1g} vibrations at 381 and 408 cm^{-1} at room temperature [28]. FTIR spectra of MoS$_2$ NF's showed the characteristic peaks of (S = O), v(Mo-O), δ(Mo-O) at 1197.53, 914, 658 cm^{-1}, respectively. MoS$_2$ NF's spectra revealed a high-frequency a band with a broad shoulder extending up to 1900 cm^{-1}, and having a weakly resolved band at roughly 1700 cm^{-1}. There are multiple bands of impurities below 1400 cm^{-1}, as well as 904 cm^{-1} for Mo-O and 595 cm^{-1} for Mo-S [29].

3.2 Structural Characterization of Aminocellulose (AC's)

Cellulose amine derivatives AC's were obtained by nucleophilic substitution reaction. Hydroxyl groups on the MCC surface were activated by tosylation of MCC. Tosylated cellulose was prepared by reacting MCC with p-toluenesuphonylchlrordie in a 1:6 ratio. Elemental analysis using a previously reported method [30] was carried out to confirm the degree of substitution. The degree of tosylation was found to be 0.48, which indicates that 50% of the OH groups were activated to be replaced. The obtained C$_{TOS}$ was then reacted with the selected amines (1:25) to substitute amines on the MCC backbone via "click chemistry. Hydroxyl groups on MCC surface were replaced by hydrazide, diethyl amine and diethyl tetraamine as shown in Scheme 1. In case of AC's, degree of amination for different amines varied between 0.40 to 0.43. AC's were watersoluble and zeta potential values confirmed that these have positive charge on its surface. Color, % yield, elemental analysis, Zeta potential, and degree of amination are presented in Table 1.

Table 1
Representing the Color, Elemental Analysis, and Degree of Substitution

	Color	Yield (%)	Elemental Analysis				Zeta Potential ζ (mV)	DS (Degree of Tosylation)	DS (Degree of Amination)
			C (Found)	H (Found)	N (Found)	S (Found)			
MCC	White powder		39.82	6.39	-	0.15	−4.24	-	-
C_{TOS}	White powder	77	45.55	5.55	5.01	4.8		0.48	-
C-Hyd	Tea pink	82	40.11	6.66	7.98	0.51	+ 32.8	-	0.41
C-DEA	Off-white	80	46.01	6.26	3.45	1.00	+ 13.9	-	0.40
C-DETA	Brown powder	89	44.01	7.71	10.55	0.66	+ 27	-	0.43

3.4 NMR of AC's

Synthesis of the AC's from MCC via tosylation was confirmed by the NMR. Figure 2 represents the ^{1}HNMR of the MCC and AC's. ^{1}HNMR and ^{13}CNMR data of the C-HYD, C-DEA, and C-DETA is represented as follows.

C-Hyd : ^{1}HNMR δ ppm; 3.10−3.00 (m, H of Cellulose), 3.23 (s, −NH$_2$), 3.91−3.46 (m, H of Cellulose), 4.36−4.20 (m, H of Cellulose), 4.69 (s, OH of Cellulose), 5.03−4.96 (d, OH of Cellulose), 5.15−5.09 (d, OH of Cellulose), 5.42 (d, anomeric H of Cellulose), 6.20 (s, −NH) ^{13}C NMR: 109.19 (anomeric), 82.31, 79.57, 76.19, 69.67.

C-DEA: ^{1}HNMR δ ppm; 5.23 (d, anomeric H of Cellulose), 5.03−4.94 (d, H of Cellulose), 4.68 (s, H of Cellulose), 4.37−4.22 (m, H of Cellulose), 3.92−3.43 (m, H of Cellulose), 3.12−3.01 (m, H of Cellulose), 2.59 (m −CH$_2$−), 1.15 (t, 6H, −CH$_3$). ^{13}C NMR: 101.74 (anomeric), 81.37, 79.16, 67.07, 62.63, 52.44 (−N−CH$_2$−), 7.95 (−CH$_3$).

C-DETA: ^{1}HNMR δ ppm;4.39−4.20 (m, H of Cellulose), 3.74−3.40 (m, H of Cellulose), 3.34−3.19 (m, H of Cellulose), 3.18−3.06 (m, H of Cellulose), 3.09−2.98 (m, H of Cellulose), 3.7 (s, −NH) 2.59−2.69 (m, 8H, CH$_2$), 1.77 (s, −NH−), 1.03 (s, −NH$_2$). ^{13}C NMR: 104.76 (anomeric), 102.84 (anomeric), 81.99, 75.13, 70.15, 69.12, 65.73, 57.18 (−CH$_2$−CH$_2$−NH−CH$_2$−CH$_2$−), 48.61, 46.79, 37.90 (−CH$_2$−CH$_2$−NH−CH$_2$−CH$_2$−).syn.

From Fig. 1 it is clear that along with the MCC backbone hydrogens distinct peaks confirming the synthesis of AC's were clearly visible in spectra. For instance, C-HYD, NH singlet appeared around 6.2ppm, while NH$_2$ hydrogens were present at 3.23ppm. CH$_3$ triplet at 1.15ppm and CH$_2$ multiplet at 2.59 indicated C-DEA successful synthesis. C-DETA synthesis was evident from NH$_2$ singlet at 1.03 ppm, NH at 1.77 ppm, CH$_2$ multiplet around 2.59-2.69ppm, followed by NH bonded to MCC at 3.7 ppm.

3.4 FTIR of AC and AC-MoS$_2$

Figure 3a) presents the FT-IR spectra of the MCC, amino cellulose derivatives AC's (C-Hyd, C-DEA, and C-DETA). Table 2 reprents the characteristic peaks observed for the AC. From Fig. 3a) and table it is evident MCC shows characteristic FTIR band positions [31]. Microcrystalline cellulose (MCC) virgin has bands of 3333 ($_{str}$OH), 2891 ($_{sym}$CH), and 1625 ($_{asym}$C−O−C). Other peaks at 1433, 1364, and 1312 are for $_{bend}$CH$_2$ and $_{wagg}$ vibrations. Skeletal vibrations of CO 1012, ß-glycosidic link 897, out of plane OH bending was at 667 cm^{-1}. In the case of the C-Hyd, C-DEA, and C-DETA. Table 2 represents the characteristic peaks observed for the AC.

Table 2
Infrared Spectral data of MCC, C-HYD, C-DEA, and C-DETA

Characteristic Wavenumber cm^{-1}					
MCC		AC			
Functional Group	Wavenumber	Functional Group	C-HYD	C-DEA	C-DETA
strOH	3333	broad $_{str}$ N−H, or −OH	3276,3325	3362	3337
					3288
CH	2891	CH	2889	2883	2897−2878
$_{asym}$C−O−C	1625	$_{asym}$C−O−C	1658	1662	1656
$_{arom}$ C−H or	1433	$_{bend}$ N−H	1589		1570
CH/CO	1364	$_{asymm,ben}$ C−H	1466	1467	1471
$_{asymm,ben}$C−H,	1312	CH/CO	1370	1375	1367
$_{str}$ C−O	1018	$_{asymm,ben}$C−H,	1314	1310	1312
bridge C-O-C sym.	897	$_{str}$C−N	1170	1166	1152
oop OH	668	$_{str}$ C−O	1032	1029	1035
		bridge C-O-C sym.	814	845	820
		oop OH	662	664	666

From Fig. 3a) and Table 2 it is clear that along with the backbone bands of MCC new bands are appearing in AC's. In C-HYD bands at 3276,3325 (N−H$_{str}$,−OH$_{str}$), 1170 (C- N $_{arom}$), 1589(NH $_{bend}$), for C-DEA bands at 3362 (OH$_{str}$), 1166 (C−N$_{str}$), and DETA bands at 3337, 3288 (NH$_{str}$, OH$_{str}$), 1570(NH$_{ben}$), and 1152(C−N$_{str}$) are of special interest. Modification of MCC in AC is confirmed by the emergence of the C−N stretch band around 1170 – 1160 cm^{-1}. This indicated that the OH group of the MCC bone is removed while amines have been decorated on the MCC backnone. For C-Hyd and C-DETA spectra the distinct change in the band intensity in the 3600 to 3200 cm^{-1} area verified the addition of NH$_2$ containing molecules on the MCC backbone by replacing OH groups. For Cell-DEA decrease in band intensity validated the substitution of -N-(CH$_2$-CH$_3$)$_2$ in place of OH. These results corroborate the NMR results.

Figure 3b) presents the AC-MoS$_2$ Nanocomposites. In AC-MoS$_2$ nanocomposites, there were found clear indications of the interaction between the MoS$_2$ NF and cellulose. For instance, in the case of MoS$_2$ and MCC bands at 1031 cm^{-1} is intensified at 1024 cm^{-1} related to anti-symmetric ring stretching is diminished, and 658 cm^{-1} related to

oop bending of OH shifted to 640 cm^{-1}, while the band at 555 cm^{-1} intensified. In the case of C-HYD-MoS$_2$, the OH band intensity is decreased at 3311 cm^{-1}, while the band at 1658 cm^{-1} is shifted to 1648 cm^{-1}, the band at 1036 is reduced in intensity and appeared at 1004 cm^{-1}, band at 619 cm^{-1}, and 567 cm^{-1} are diminished, implying that the NH$_2$ and O-H are involved in an interaction with the MoS$_2$ NFs. In the case of C-DEA-MoS$_2$, the broad band of O-H region 3370 cm^{-1} becomes less intensified and appeared at 3354 cm^{-1}, the band at 1654 cm^{-1} become rudimentary, while C-O-C band appears at 1026 cm^{-1} shifted to 1006 cm^{-1}. This can be attributed to the involvement of the O-H of MCC backbone is involved in the interaction with MoS$_2$ NF's. In case of C-DETA-MoS$_2$, the results were quite interesting, a very low-intensity band at 3280 cm^{-1} O-H/N-H was found, whereas bands at 1656 were found at 1642 cm^{-1} with a very low-intensity similar band at 1024 was found at 1006 cm^{-1}. The presence of band position between 1170 to 1160 cm^{-1} related to C-N confirmed that during all the modifications to obtain MoS2-loaded amino cellulose derivatives amines are decorated on the MCC backbone. Figure 3b) represents the MoS$_2$ NF loaded AC's there is a clear change in the intensity of the band position in the O-H and N-H bond area which imply the occurrence of bonding between the MoS$_2$ NFs and amino cellulose. Skeletal vibration related to C-O also lowered in intensity verifying the interaction between the MoS$_2$ NF and the polymer. Shifting of the C-O vibrations to the lower wavenumber indicates strong hydrogen bonding between amino cellulose and MoS$_2$ [32]. Reduction in the band position at 1654 cm^{-1} ascribed to in-plane bending of NH$_2$ not only reduced but showed a shift in the position indicating the MoS$_2$ NF and ligand coordination by the amine group. Moreover in literature, band broadness around 1650 cm^{-1} is indicative of S-O stretch. Bands around 650 cm^{-1} represent the interaction of cellulose with Mo-S as explained in literature [33].

3.4 XRD structure of AC and AC-MoS$_2$

Figure 4 represents the crystallographic structure of the amino cellulose derivatives and AC-MoS$_2$ nanocomposites. MCC was found to be having cellulose type I crystallographic patterns without any doublet in the main peak intensity [18, 34]. MCC has characteristics peaks related to semicrystalline monolithic cellulose type I planes at 2θ = 15.43°, 16.21°, 22.4°, and 34.7° corresponding to the crystallographic planes (110)/(110$^-$), (200), and (004). The surface of the 200 is hydrophobic while the surface of the (110)/(110$^-$) planes is hydrophilic [35]. AC has diffraction pattern showing an amorphous structure resulting from the dissolution and chemical modification at 80°C. Diffraction pattern of amino cellulose C-Hyd, C-DEA, and C-DETA at angles 2 θ = 20.6°, 22°, 34.8°, 2 θ = 20.5°, 22.1°, 36.5°, and 2 θ = 20.6°, 22.3°, 35.1°, demonstrate the coexistence of Cellulose I and Cellulose II. For AC-MoS$_2$ nanocomposites, both the amino cellulose derivatives peaks and MoS$_2$ peaks were present. Similar results were observed in the case of g-C$_3$N$_4$/MoS$_2$ composites [23]. In Cell-Hyd-MoS$_2$, derivatives peaks at 22.5° (200) have increased in intensity while at 33.6° (100) and 59.0°(110), peak-related MoS$_2$ was observed. In C-DEA-MoS$_2$, XRD pattern, there was a peak around 22.5° (200) area was still a broad halo, and at 33.6° (100) peak related to MoS$_2$ was present. In C-DETA- MoS$_2$, the Peak related to Cellulose at 22.5° (200) increased in intensity while MoS$_2$ presence was confirmed by a peak around 33.6° (100). From these results, we infer that the MoS$_2$ has been successfully adsorbed on the Amino cellulose derivatives. Furthermore, MoS$_2$ NFs are not only adsorbed but are acting as anchoring sites for the cellulose chains leading to a more crystalline structure as indicated by the increase in the intensity of the peaks for (200) planes around 22.5°. The slight difference between the pristine MoS$_2$ and MCC indicates the assembly and rearrangement during the adsorption process. After nanocomposite formation, the MoS$_2$ crystal plane peak shows a slight shifting as in the case of Cellulose/ MoS$_2$ [36].

3.5 SEM structure of AC and AC-MoS$_2$

SEM micrographs were captured to understand the surface morphology of MoS$_2$, MCC, and AC-MoS$_2$ nanocomposites as shown in Fig. 5. MCC was showing a short rod like morphology under SEM [37]. MoS$_2$ nanospheres look like a plump and thin fluffy flower as shown in Fig. 5b) [38]. In Fig. 5c-e) amino cellulose derivatives have a smooth surface with highly interconnected structure. There was homogeneous amination of cellulose with a consistent morphology. The dissolution, and freeze drying of the amino cellulose derivatives and adsorption of MoS$_2$ have altered the surface morphology. Moreover, the MoS$_2$ have tightly anchored the surface of the Amino cellulose derivatives as shown in Fig. 5f-k). As anticipated the MoS$_2$ NFs were visible on the surface randomly distributed on the surface. Cell-Hyd-MoS$_2$, and Cell-DETA-MoS$_2$ has a homogenous rough structure where the MoS$_2$ NFs are on the different layers of the amino cellulose backbone, while Cell-DEA-MoS$_2$ has clusters on the surface of MoS$_2$ NFs. It is clear that the concentration was under critical concentration which was enough to have the random distribution and no agglomeration was observed. Energy disperse X-ray spectroscopy (EDS) as shown in Fig. 5l-n) also reinforced the adsorption of MoS$_2$ on amino cellulose by showing corresponding Mo, S, C, and N element detection in sample. In case of MCC/MoS$_2$/Fe$_3$O$_4$, MoS$_2$ and Fe$_3$O$_4$ nanoparticle adsorption on polymer surface made the nanocomposites surface rough [39]. In another report, many MoS$_2$ nanosheets were adsorbed on cellulose surface [40].

3.6 Zeta potential values of AC and AC-MoS$_2$

Zeta potential values of MoS$_2$ NFs were found to be -16 mV. While the Zeta potential values of the MCC were found − 4.24, Cell-HYD + 32.8, Cell-DEA + 13.9, and Cell-DETA + 27 mV. Zeta potential values shift confirmed the successful amination of MCC, these amine groups on the surface of the MCC resulted in the cationic character of the amino cellulose derivatives [25]. MoS$_2$ has a negative charge on its surface [41], we expected that the electrostatic force of attraction between the AC and MoS$_2$ NFs is the binding force on the surface of amino cellulose [10]. These results corroborate the SEM results where MoS$_2$ NFs are found tightly anchored on its surface. Brownian motions and oppositely charged surface potentials governed the heterocoagulation of MoS$_2$ onto cationic amino cellulose backbone. The cationic amino cellulose was found to aggregate in the presence of MoS$_2$ due to the reduced net charge of the colloidal suspensions [42, 43].

3.7 Swelling and degradation studies of AC and AC-MoS$_2$

Swelling analysis of the materials for tissue engineering describes the solute substrate interaction such as solute diffusion, surface chemistry, and solvent retaining capacity. Swelling is important as it gives information about the interaction of the body fluid and the polymer composites [44]. MCC is hydrophilic, while amine derivatives also exhibited swelling. The addition of MoS$_2$ NF's on the surface of AC's fine-tuned the swelling ratio of the AC-MoS$_2$. The swelling trend is shown in Fig. 6a). AC MoS$_2$ exhibited slightly higher swelling as compared to the MCC. A similar increase in swelling was observed in the case of Carboxymethyl Cellulose/β-Cyclodextrin/Chitosan with magnetic nanoparticles hydrogel exhibited [45]. GO/MoS$_2$-PVA composite revealed a limited increase in swelling ratios where Mo and S atoms increased the water permeability [46].

Degradation studies elucidate the rate at which ACs and AC-MoS$_2$ will degrade in a physiological environment. Figure 6b) represents the mass remaining at different time intervals. Polymers are large molecules and show

degradation by extracellular enzymes [47]. AC and AC-MoS$_2$ were incubated with collagenase type II for 24 hours and the remaining mass was evaluated. MCC degraded faster as compared to the AC with MoS$_2$ NF's. MoS$_2$ NF's acted as a nucleating site for the polymer chains and because of increased crystallinity, the AC-MoS$_2$ composites acted stable. Moreover, MoS$_2$ acts as an enzymatic inhibitor and resists enzymatic degradation [48].

3.8 Cell culture studies of AC and AC-MoS$_2$

Negatively charged surface of the MoS$_2$ impede its efficacy against negatively charged surfaces such as cancer cells [49]. As a result, one method to fully exploit MoS$_2$ NF's anticancer potential is to mix it with a cationic, biocompatible anticancer agent. One such example is Chitosan/MoS$_2$ nanocomposites with remarkable bactericidal capability and excellent biological compatibility [50]. In another instance, MoS$_2$ nanosheets were coated with amino-contained poly((polyethylene glycol) methyl ether methacrylate) (PPEGMA) for drug delivery and photothermal cancer treatment [51]. Therefore we fabricated cationic charge containing AC's adsorbed with the MoS$_2$ NF's to use as anticancer therapeutics. To validate our hypothesis we first evaluated the cytotoxicity against four different cell lines against AC's and then varied the MoS$_2$ concentration from 10, 20,30, 40, 50, 60, 80, and 100μg/mL adsorbed on AC's to get the IC$_{50}$ of MoS$_2$ effective in combination with AC's.

IC$_{50}$ (half maximal inhibitory concentration)

AC cytotoxicity was assessed by adding serially diluted concentrations of derivatives to four different cell lines such as NIH3T3, B16F10, MDA-MB-231, and MCF-7 in a 96-well plate. IC$_{50}$ curves were plotted, and these dose-response curves revealed amino cellulose is found selectively cytotoxic against cancer cell by inhibiting metabolic activity as shown in Fig. 6c). From Fig. 6c) Based on IC$_{50}$ values, for NIH3T3 (263.9 μg/mL), B16F10 (207 μg/mL), MDA-MB-231 (201.6 μg/mL), and MCF-7 (238.9 μg/mL), MCC was not found cytotoxic to any cell line. Amino cellulose derivatives showed the following cytotoxicity trend

MCC   Cell DEA   Cell Hyd   Cell DETA.

While the cell lines have the following sensitivity order

B16F10   MCF-7   MDA-MB-231   NIH3T3.

For B16F10 we had the IC$_{50}$ between 130 to 101μg/mL. Cell DETA outperformed Cell Hyd in anticancer activity against melanoma and breast cancer cell lines, where IC$_{50}$ values were found between 75 μg/mL and 101μg/mL.

From this data we took 200 μg/mL was safe concentration against the NIH3T3 cells and below this value, the AC's were selectively cytotoxic against B16F10, MDA-MB-231, and MCF-7, as reported previously [52].

Effective MoS$_2$ concentration with IC$_{50}$ of AC

Figure 6d, e, and f) represent the concenteration of MoS$_2$ in combination with AC's, to evaluate the IC$_{50}$ (half maximal inhibitory concentration) of the AC-MoS$_2$. To check the effect of MoS$_2$ NF's on the cytotoxicity, we added MoS$_2$ from 10, 20, 30, 40, 60, 80, 100, 200, 250, 500, and 600 μg/mL and plotted IC$_{50}$ curves. From the analysis of IC$_{50}$ curves against four cell lines, we found that the cells were sensitive to the dose-dependent response of MoS$_2$. The cytotoxicity effect of AC's-MoS$_2$ derivatives was increased as compared to the AC's alone. Figure 6d) indicated that for B16F10, against Cell-Hyd 32 ug/mL of MoS$_2$, for Cell-DEA 32 μg/mL of MoS$_2$, for Cell-DETA 38 μg/mL of

MoS$_2$ was found at IC$_{50}$. Similarly, Fig. 6e) showed that for the MCF-7 cell line, 33, 34, and 32 μg/mL of MoS$_2$ with Cell-Hyd, Cell-DEA, and Cell-DETA were found respectively, at IC$_{50}$. Figure 6f) showed that in the case of MCF-7 30, 36, 37 μg/ mL of the MoS$_2$ with Cell-Hyd, Cell-DEA, and Cell-DETA, was found effective at IC$_{50}$.

Further, the cytotoxicity and proliferation inhibition for day 1 to day 3 of MoS$_2$ labeled nanocomposites was carried out by adding 1, 3, and 5 wt % of MoS$_2$ in amino cellulose. These nanocomposites were also monitored against four cell lines, as shown in Fig. 7a, b, c, and d).

In Fig. 7a) or the three days trials in case of AC's with MoS$_2$ 1wt% cells viability decreased from 85–20%, while for 5wt % these values decreased to 12%. In the case of amino cellulose, the cell viability was up to 80% on day 1 when concentration of MoS$_2$ was up to 3%. For 5wt% cell viability changed from 70% on day 1 to 16% on day 3.

Cell DETA has cell viability on day 1 at around 80% which decreased to around 16–20% on day 3. The lowest cell viability was for Cell DEA at 5wt% when 67% of cells survived.

In case of B16F10 cell line, we had the most promising results. Cell viability percentage was as high as 20% for MCC-HYD-MoS$_2$ at 5wt%, Cell Hyd and DETA have 18 to 15% cell viability at all MoS$_2$ loadings, on day 1. For day 3 the cell viability was lowest for Cell DETA at 5 wt %, while all other amino cellulose MoS$_2$ derivatives have cell viability of 6–7%. For MDA-MB-231 cells as in Fig. 7c), interesting results were obtained. On day 1, cell viability was from 28–64%. On day 3, the cell viability was lowest at 19%. While Cell DETA had the minimum cell viability of 12%, for 5wt% MoS$_2$ loadings. Figure 7d) For the MCF-7 cell line 24 hour contact time was found effective, for instance in Cell-HYD we have 30% cell viability on 1% MoS$_2$ loadings, while 29% for 5wt% MoS$_2$ loading. On day 3 cell viability decreased to 16 and 13% for the same above loadings. poly(2-aminoethyl methacrylate) (poly(AEM))and poly(N-(2-aminoethylmethacrylamide) (poly(AEMA)) deposited with gold nanoparticles showed decreased cell viability of J774A1 (mouse monocyte cells)and MCF-7 (human breast adenocarcinoma cells)and were found suitable for biomedical applications [43]. carboxymethyl cellulose and silver nanoparticles (CMC-AgNPs)based nanocomposites exhibited a strong cytotoxic effect on liver cancer cells (HepG2). hydroxypropyl cellulose (HPC), or hydroxypropyl methylcellulose (HPMC) with silver [53].

LIVE/DEAD staining

LIVE/DEAD assay depicts the chromatin and morphology of the cells which is a reliable indicator of healthy, apoptotic, and necrotic cells. Through microscopic examination of Calcein-AM (live cells fluorescent green, indicating intracellular esterase activity) and ethidium homodimer (dead cells fluorescent as red, indicating loss of plasma membrane activity) stained cells, the apoptosis induction properties of the samples after treatment of the fibroblast (NIH3T3), melanoma (B16F10), human epithelial adenocarcinoma (MDA-MB-231), and human breast adenocarcinoma (MCF-7) cell line were examined in this study. Figure 8a, b, c, and d) displays representative microscopic pictures of LIVE/DEAD stained cells after being exposed for 24 hours to MCC, Cell-Hyd, Cell-DEA, and Cell-DETA with 5wt% MoS$_2$ as found effective in the previous experiment against four cell lines. Apoptotic cells (red) are visible in both AC's but cell death was found higher in the case of MoS2-loaded AC's, as shown in Fig. 8. While a higher number of viable cells are visible in AC's derivatives, it appears that MoS$_2$ loaded AC's cause more cell death exposing the DNA/chromatin to bind with the ethidium homodimer, than free AC's does at the same time IC$_{50}$. While both control and AC's treated cells did not exhibit a significant amount of cell death.

According to our findings, we suggest that the AC's with MoS_2 NFs provide a reliable anticancer delivery system. In vitro testing compared the cytotoxicity of the pristine amino cellulose derivatives has improved efficacy with MoS_2 NF's concentration. Therefore, it can be asserted that when higher doses of MoS_2 NFs 5wt% are used, the administration dose for developed AC's can be decreased to have an effective clinical response. The dose-dependent side effects are also thought to be lessened. We suppose that our MoS_2 decorated AC's can be used as cancer theranostics.

Conclusion

In this work, we have presented a comprehensive account of the synthesis of AC's derivatives via tosylation followed by amine functionalization leading to 6-deoxy-6-hydrazide cellulose, 6-deoxy-6-(N, N-diethyl) amine cellulose, and 6-deoxy-6-diethyl triamine cellulose (C-Hyd, C-DEA, and C-DETA). The resulting AC's were decorated with MoS_2 and characterized by using a combination of analytical, spectroscopic, and microscopic techniques. The anionic surfaces of unmodified MCC were rendered cationic after the synthesis. MoS_2 nanoflowers were deposited on the cationic amino cellulose surfaces, as illustrated by SEM and XRD analysis. The results of the Prestoblue assay indicated that the cationic modified AC's derivatives after MoS_2 loading decreased the cell viability at higher concentrations sucha s 5wt%, leading to more suitable nanocomposites for cancer therapy biomedical applications. Furthermore, the melanoma B16F10 melanoma cells were most sensitive followed by the MCF-7 cell line and MDA-MB-231.

Declarations

Ethics approval and consent to participate

Ethical approval is not required for this typr of research work.

Consent for publication

All the authors give their consent for the publication of identifiable details, which can include photograph(s) and/or details within the text to be published in this Journal .

Availability of data and materials

No other data is involved in this research work.

Competing Interests

The authors declare no competing interest.

Acknowledgement

Author Contributions

References

1. Navya, P., et al., *Current trends and challenges in cancer management and therapy using designer nanomaterials*. 2019. **6**(1): p. 1–30.

2. Sabir, F., et al., *How to face skin cancer with nanomaterials: A review*. 2021. **11**: p. 11931–11955.

3. Cheng, Z., et al., *Nanomaterials for cancer therapy: Current progress and perspectives*. 2021. **14**(1): p. 1–27.

4. Shcharbin, D., et al., *Hybrid metal-organic nanoflowers and their application in biotechnology and medicine*. Colloids and Surfaces B: Biointerfaces, 2019. **182**: p. 110354.

5. Zhang, M., et al., *Enzyme-inorganic hybrid nanoflowers: Classification, synthesis, functionalization and potential applications*. Chemical Engineering Journal, 2021. **415**: p. 129075.

6. Liu, Y., X. Ji, and Z. He, *Organic–inorganic nanoflowers: from design strategy to biomedical applications*. Nanoscale, 2019. **11**(37): p. 17179–17194.

7. Liu, T., et al., *Ultra-small MoS2 nanodots with rapid body clearance for photothermal cancer therapy*. 2016. **9**(10): p. 3003–3017.

8. Zhu, X., et al., *Intracellular mechanistic understanding of 2D MoS2 nanosheets for anti-exocytosis-enhanced synergistic cancer therapy*. 2018. **12**(3): p. 2922–2938.

9. Murugan, C., et al., *Two-dimensional cancer theranostic nanomaterials: Synthesis, surface functionalization and applications in photothermal therapy*. 2019. **299**: p. 1–20.

10. Nazir, F., M.J.R. Iqbal, and F. Polymers, *Piezoelectric MoS2 nanoflowers (NF's) for targeted cancer therapy by gelatin-based shear thinning hydrogels. In vitro and in vivo trials*. 2022: p. 105435.

11. Feng, W., et al., *Flower-like PEGylated MoS2 nanoflakes for near-infrared photothermal cancer therapy*. 2015. **5**(1): p. 1–13.

12. Wang, J., et al., *MoS2-based nanocomposites for cancer diagnosis and therapy*. 2021. **6**(11): p. 4209–4242.

13. Seddiqi, H., et al., *Cellulose and its derivatives: Towards biomedical applications*. 2021. **28**(4): p. 1893–1931.

14. Alibolandi, M., et al., *Carbohydrate-Based Materials in Tissue Engineering Applications*. 2022: p. 1–31.

15. Nazir, F., et al., *6-deoxy-aminocellulose derivatives embedded soft gelatin methacryloyl (GelMA) hydrogels for improved wound healing applications: In vitro and in vivo studies*. 2021. **185**: p. 419–433.

16. Meng, L.-Y., et al., *Cellulose-based nanocarriers as platforms for cancer therapy*. 2017. **23**(35): p. 5292–5300.

17. Shi, W., Y.C. Ching, and C.H.J.I.j.o.b.m. Chuah, *Preparation of aerogel beads and microspheres based on chitosan and cellulose for drug delivery: A review*. 2021. **170**: p. 751–767.

18. Rafieian, F., et al., *Amine functionalization of microcrystalline cellulose assisted by (3-chloropropyl) triethoxysilane*. 2019. **130**: p. 280–287.

19. Shokri, M., et al., *A novel amino cellulose derivative using ATRP method: Preparation, characterization, and investigation of its antibacterial activity.* 2021. **106**: p. 104355.

20. Cheng, F., et al., *Synthesis and antibacterial effects of aqueous colloidal solutions of silver nanoparticles using aminocellulose as a combined reducing and capping reagent.* 2013. **15**(4): p. 989–998.

21. Wen, X., et al., *In vitro and in vivo investigation of bacterial cellulose dressing containing uniform silver sulfadiazine nanoparticles for burn wound healing.* 2015. **25**(3): p. 197–203.

22. Zhou, C., et al., *Bi2S3@ MoS2 Nanoflowers on Cellulose Fibers Combined with Octahedral CeO2 for Dual-Mode Microfluidic Paper-Based MiRNA-141 Sensors.* 2021. **13**(28): p. 32780–32789.

23. Nouri, A., et al., *Simultaneous linear release of folic acid and doxorubicin from ethyl cellulose/chitosan/g-C3N4/MoS2 core-shell nanofibers and its anticancer properties.* 2021. **109**(6): p. 903–914.

24. Wu, J.M., et al., *Piezo-catalytic effect on the enhancement of the ultra-high degradation activity in the dark by single-and few-layers MoS2 nanoflowers.* 2016. **28**(19): p. 3718–3725.

25. Nazir, F. and M.J.P. Iqbal, *Synthesis, characterization and cytotoxicity studies of aminated microcrystalline cellulose derivatives against melanoma and breast cancer cell lines.* 2020. **12**(11): p. 2634.

26. Liu, B., et al., *Synthesis and optimization of MoS2@ Fe3O4-ICG/Pt (IV) nanoflowers for MR/IR/PA bioimaging and combined PTT/PDT/chemotherapy triggered by 808 nm laser.* Advanced Science, 2017. **4**(8): p. 1600540.

27. Li, W., et al., *Magnetic assembly synthesis of high-efficiency recyclable flower-like MoS2@ Fe3O4@ Cu2O like-Z-scheme heterojunction towards efficient photodegradation of tetracycline.* 2021. **555**: p. 149730.

28. Kwak, J.Y.J.R.i.P., *Absorption coefficient estimation of thin MoS2 film using attenuation of silicon substrate Raman signal.* 2019. **13**: p. 102202.

29. Peng, W., et al., *Fabrication of 3D flower-like MoS2/graphene composite as high-performance electrode for capacitive deionization.* Desalination, 2020. **473**: p. 114191.

30. EL-Sayed, N.S., et al., *Syntheses of New Antimicrobial Cellulose Materials Based 2-((2-aminoethyl) amino)-4-aryl-6-indolylnicotinonitriles.* 2017. **60**(3): p. 465–477.

31. Chen, J., et al., *Preparation and performance of thermoplastic starch and microcrystalline cellulose for packaging composites: Extrusion and hot pressing.* 2020. **165**: p. 2295–2302.

32. Song, Y., et al., *Porous cellulose composite aerogel films with super piezoelectric properties for energy harvesting.* 2022. **288**: p. 119407.

33. Yao, G., et al., *La (OH) 3 synergistically reinforced hierarchical MoS2@ Cellulose-Lignin composite membranes for tellurium (IV) separation in wastewater.* 2022. **372**: p. 133787.

34. Terinte, N., R. Ibbett, and K.C.J.L.B. Schuster, *Overview on native cellulose and microcrystalline cellulose I structure studied by X-ray diffraction (WAXD): Comparison between measurement techniques.* 2011. **89**(1): p. 118–131.

35. Ye, D., et al., *Preferred crystallographic orientation of cellulose in plant primary cell walls.* 2020. **11**(1): p. 1–10.

36. Wu, T., et al., *High-performance nanogenerators based on flexible cellulose nanofibril/MoS2 nanosheet composite piezoelectric films for energy harvesting.* 2021. **80**: p. 105541.

37. Kong, X., et al., *Antibacterial polyvinyl alcohol films incorporated with N-halamine grafted oxidized microcrystalline cellulose.* 2019. **15**: p. 25–29.

38. Ma, J., et al., *Embedded MoS2-PANI nanocomposites with advanced microwave absorption performance.* 2020. **198**: p. 108239.

39. Gao, P., et al., *Self-assembled magnetic microcrystalline cellulose/MoS2/Fe3O4 composite for efficient adsorptive removal of mercury ions (Hg2+)*. 2021. **25**: p. 100736.

40. Uddin, A., et al., *Waste paper cellulose based-MoS2 hybrid composites: Towards sustainable green shielding.* 2022. **31**: p. 103858.

41. Lin, H.-Y., et al., *Systematic investigation of the piezocatalysis–adsorption duality of polymorphic MoS2 nanoflowers*. 2022. **317**: p. 121717.

42. Koshani, R., M. Tavakolian, and T.G.J.J.o.M.C.B. van de Ven, Cellulose-based dispersants and flocculants. 2020. **8**(46): p. 10502–10526.

43. Hemraz, U.D., et al., *Cationic poly (2-aminoethylmethacrylate) and poly (N-(2-aminoethylmethacrylamide) modified cellulose nanocrystals: synthesis, characterization, and cytotoxicity*. 2015. **16**(1): p. 319–325.

44. Nazir, F., et al., *Fabrication of robust poly L-lactic acid/cyclic olefinic copolymer (PLLA/COC) blends: study of physical properties, structure, and cytocompatibility for bone tissue engineering*. 2021. **13**: p. 1732–1751.

45. Naderi, Z., et al., *Synthesis and characterization of carboxymethyl cellulose/β-cyclodextrin/chitosan hydrogels and investigating the effect of magnetic nanoparticles (Fe3O4) on a novel carrier for a controlled release of methotrexate as drug delivery*. 2020. **30**(4): p. 1339–1351.

46. Yadav, S., et al., *Feasibility of brackish water and landfill leachate treatment by GO/MoS2-PVA composite membranes*. 2020. **745**: p. 141088.

47. Erdal, N.B. and M.J.B. Hakkarainen, *Degradation of cellulose derivatives in laboratory, man-made, and natural environments*. 2022. **23**(7): p. 2713–2729.

48. Ikram, M., et al., *MoS 2/cellulose-doped ZnO nanorods for catalytic, antibacterial and molecular docking studies*. 2022. **4**(1): p. 211–225.

49. Pillai, P.P., et al., *Engineering gram selectivity of mixed-charge gold nanoparticles by tuning the balance of surface charges.* 2016. **55**(30): p. 8610–8614.

50. Cao, W., L. Yue, and Z.J.C.p. Wang, High antibacterial activity of chitosan–molybdenum disulfide nanocomposite. 2019. **215**: p. 226–234.

51. Zeng, G., et al., *Mussel inspired preparation of MoS2 based polymer nanocomposites: The case of polyPEGMA*. 2016. **387**: p. 399–405.

52. Nazir, F. and M. Iqbal, *Synthesis, characterization and cytotoxicity studies of aminated microcrystalline cellulose derivatives against melanoma and breast cancer cell lines*. Polymers, 2020. **12**(11): p. 2634.

53. Salem, S.S., et al., *Synthesis of silver nanocomposite based on carboxymethyl cellulose: Antibacterial, antifungal and anticancer activities*. 2022. **14**(16): p. 3352.

Scheme

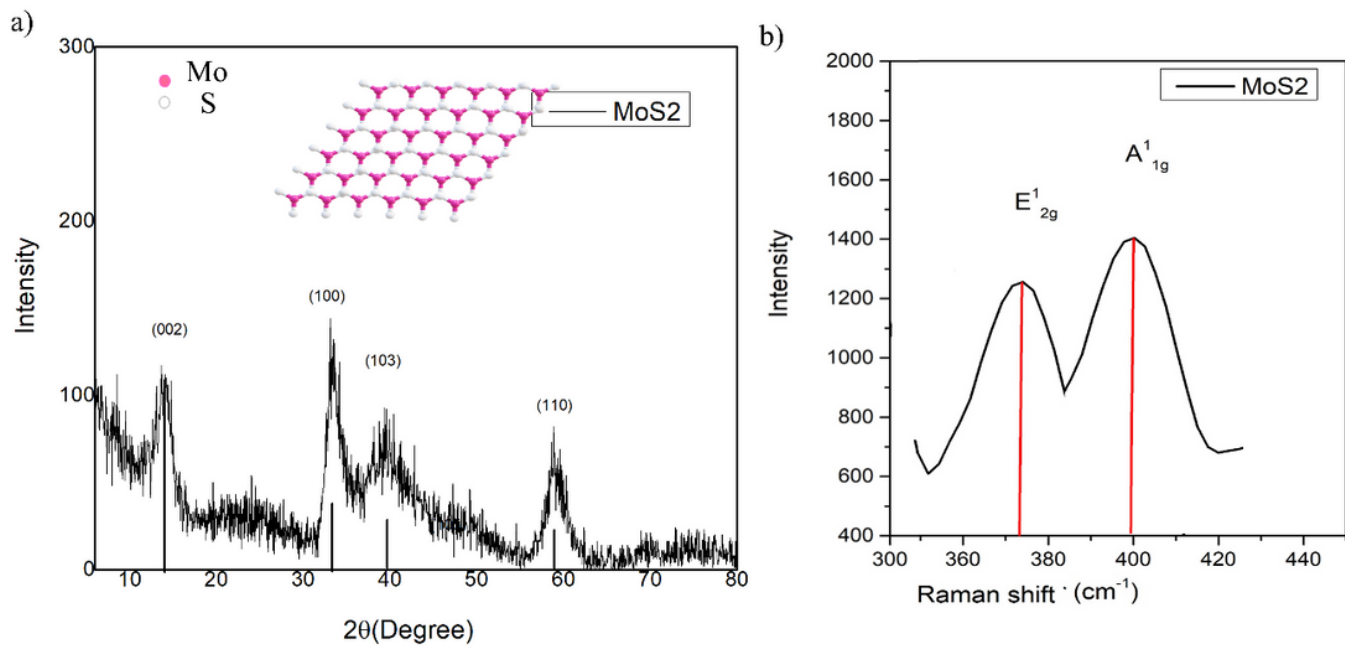Scheme 1 is available in supplementary section.

Figures

Figure 1

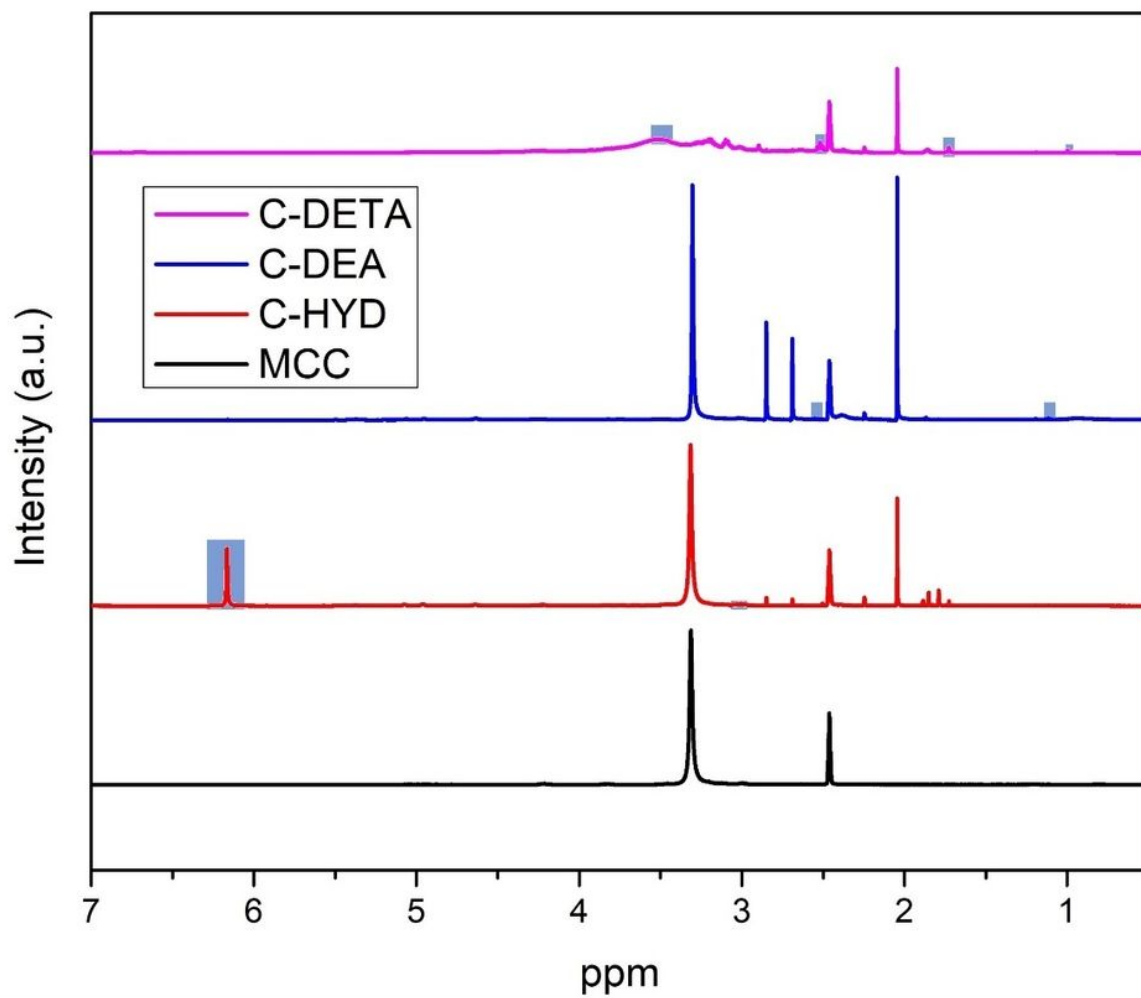a) Showing XRD pattern of MoS_2 b)Raman spectrum of MoS_2
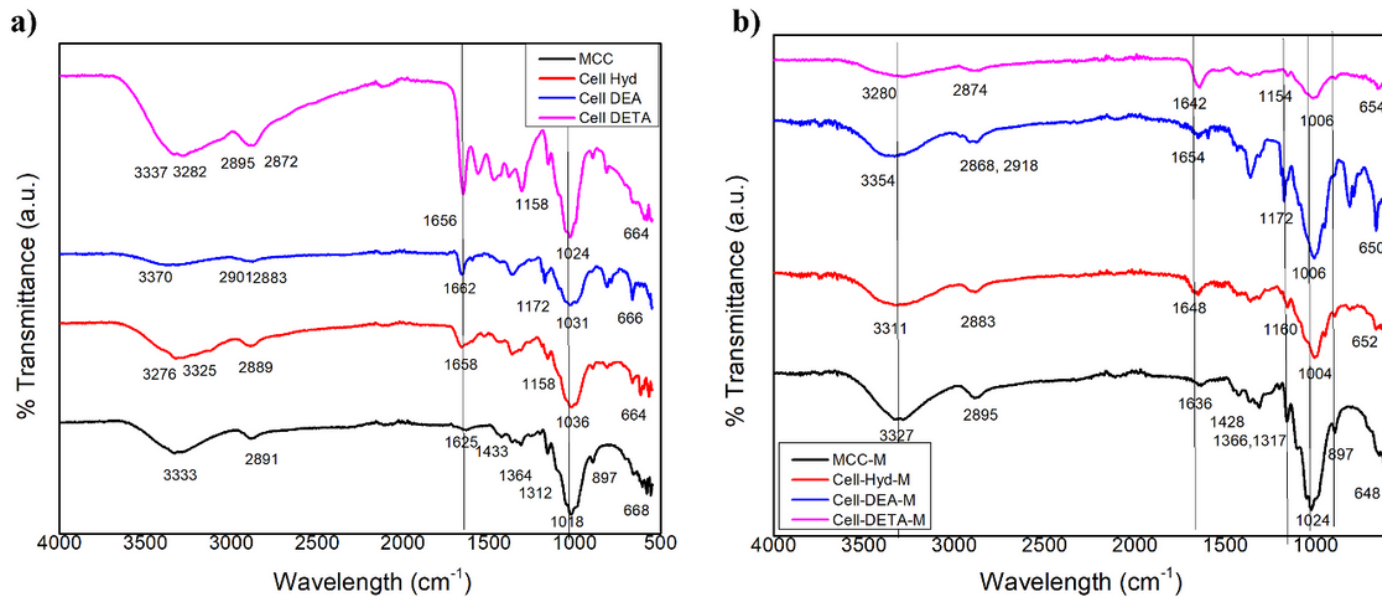
Figure 2

^{1}HNMR of MCC and AC's

Figure 3

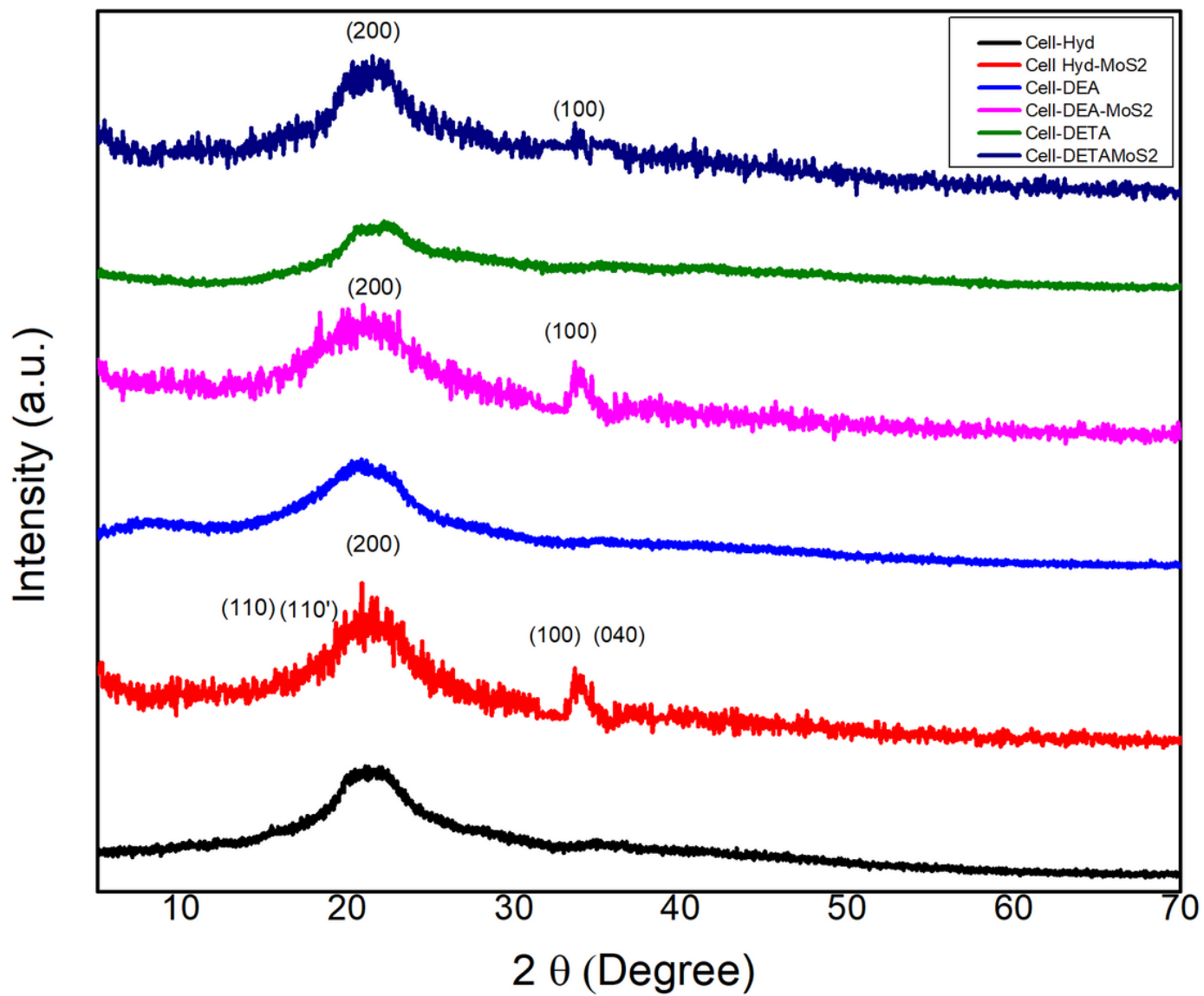FTIR a) AC's derivatives b) MoS$_2$ labeled Amino cellulose derivatives
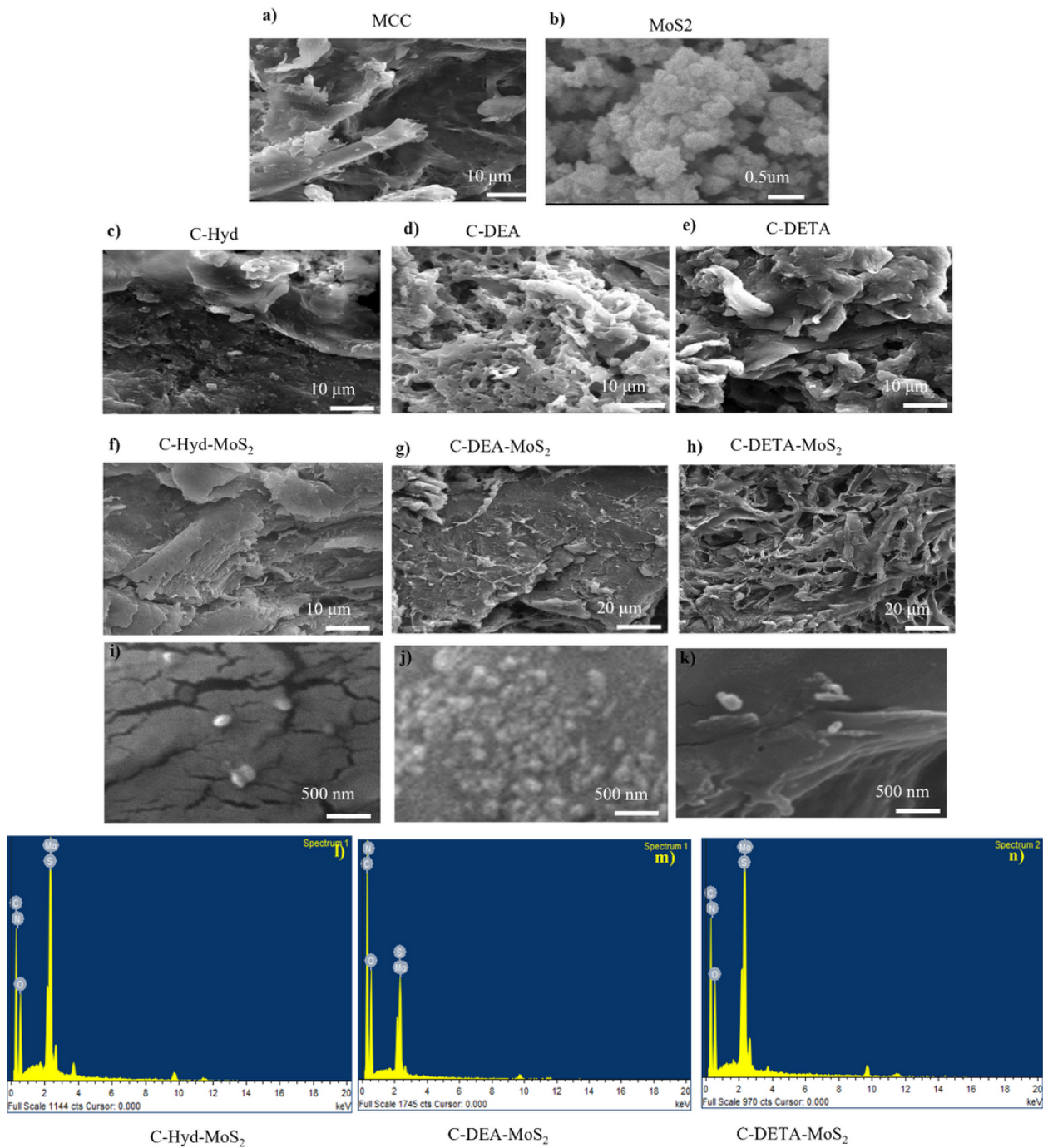
Figure 4

XRD pattern of AC's and AC-MoS$_2$

Figure 5

SEM images of a) MCC, b) MoS$_2$, c-e) amino cellulose derivatives,f-k)Ac- MoS$_2$ composites at 10µm and 500 nm. l-n) EDS spectra of AC-MoS$_2$
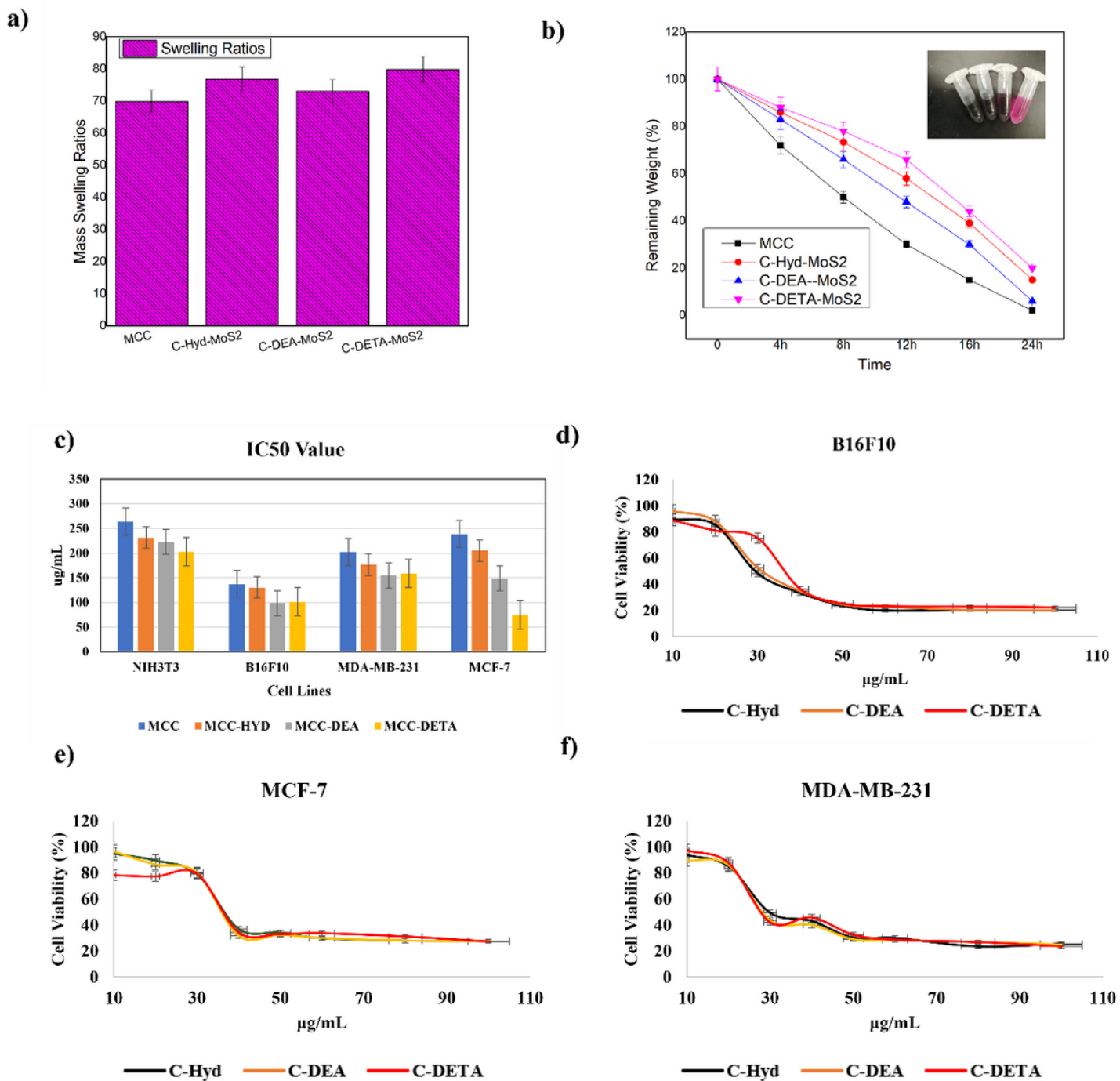
Figure 6

a) Swelling ratios, b) degradation rate, c) IC$_{50}$ values for AC's, and d) IC$_{50}$ values of the AC's and MoS$_2$ (dose-dependent response of MoS$_2$ with different amino celluloses).
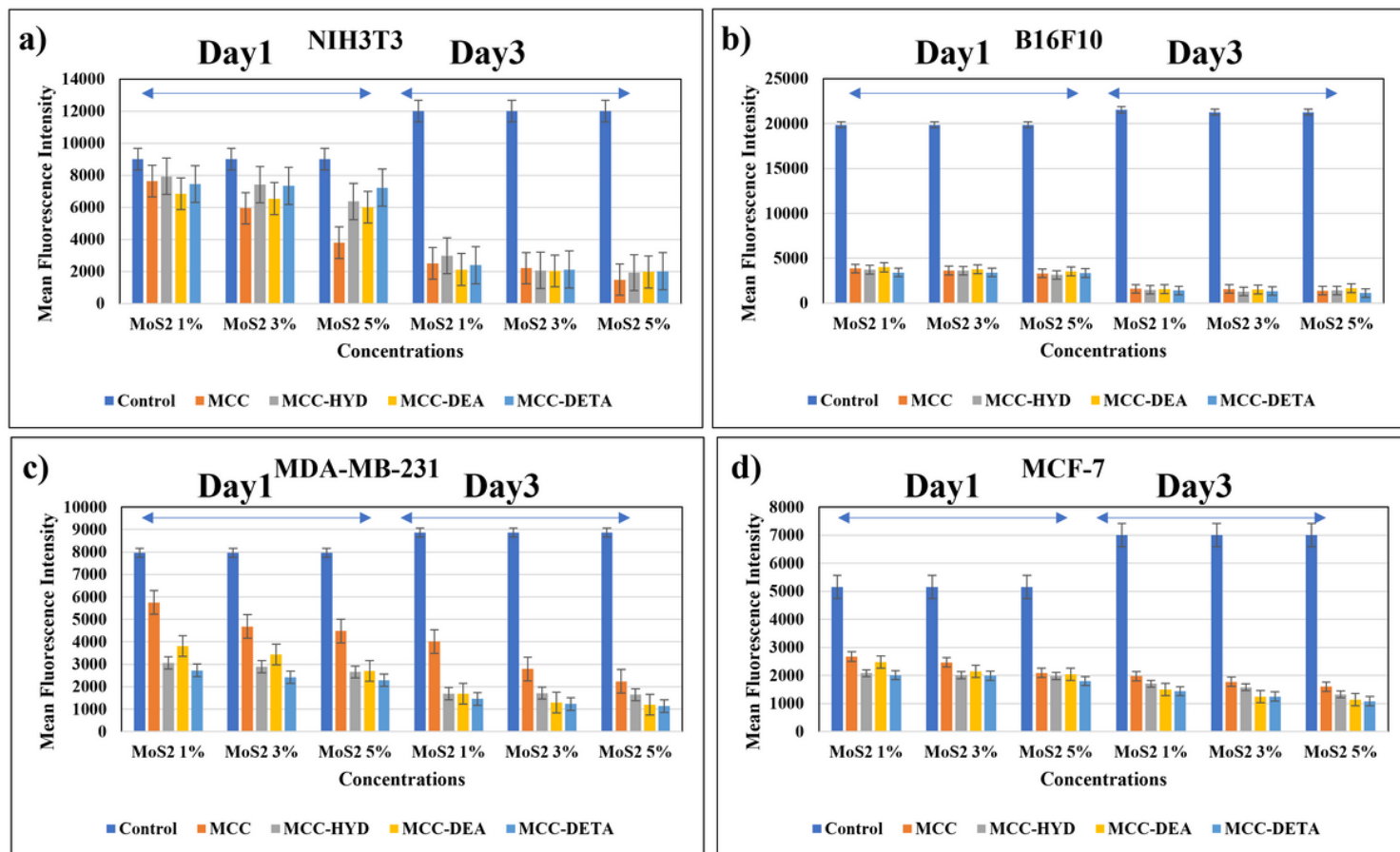
Figure 7

Cytotoxicity of AC-MoS$_2$ with 1, 3, and 5wt% of MoS2 adsorbed on the AC surface. cell fluorescence intensity using presto blue assa indicates the cell viability for a) NIH3T3, b) B16F10, c) MDA-MB-231, d) MCF-7.
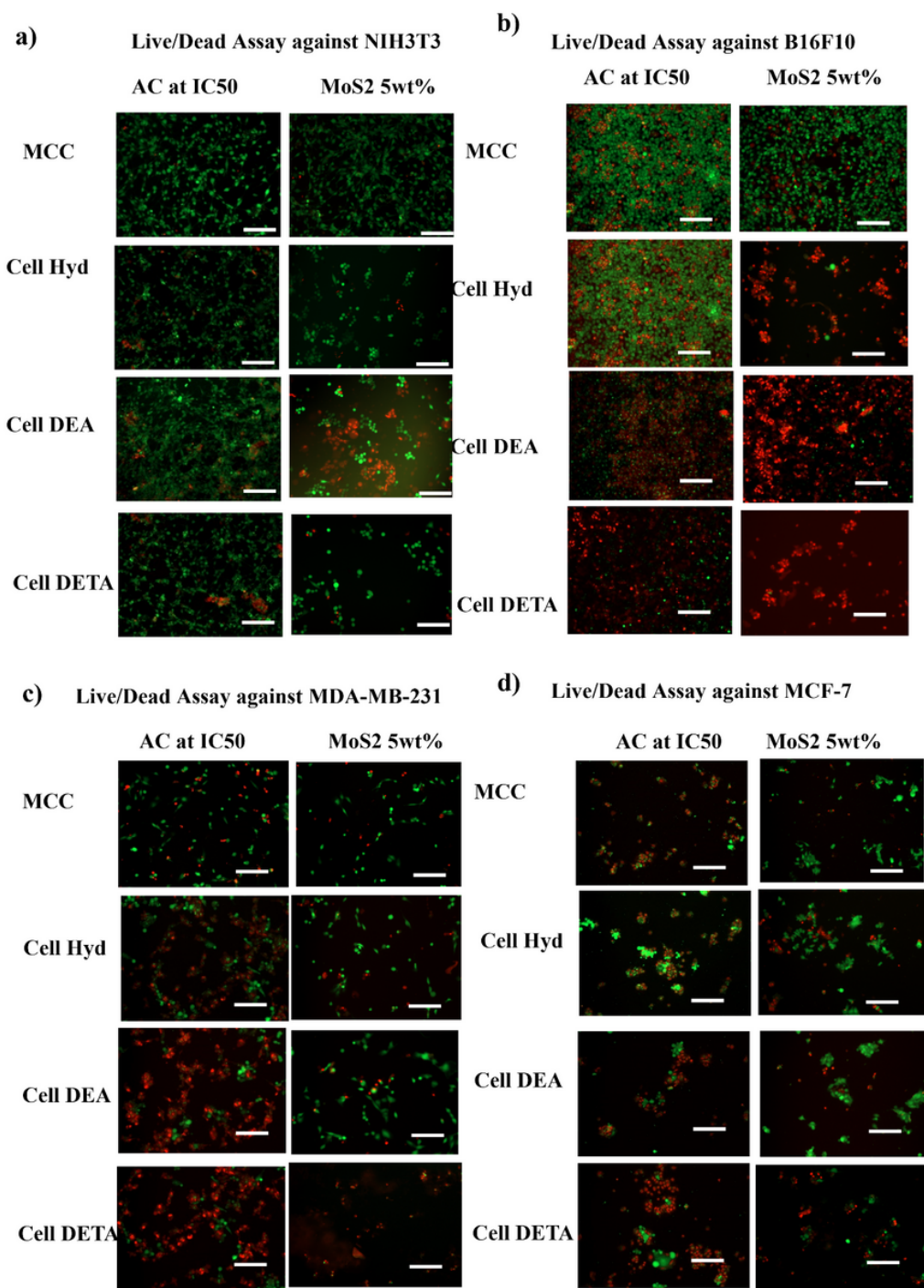
Figure 8

Cell viability of ACs and ACs-MoS$_2$ nanocomposites against four cell lines a) NIH3T3 b) B16F10, c) MDA-MB-231, d) MCF-7.

Supplementary Files

This is a list of supplementary files associated with this preprint. Click to download.

- floatimage1.png